Journal of Structural and Construction Engineering, 13(02), 2026, pp. 5-24

Journal of Structural and Construction Engineering

www.jsce.ir

Computational Fluid Dynamics Evaluation of Vortex-Induced Vibrations in Single and Multiple Cylinders for Offshore Design

Seyed Reza Samaei [1], Mohammad Asadian Ghahfarokhi [2]*

1- Assistant professor, Department of Civil Engineering, SR.C., Islamic Azad University, Tehran, Iran; samaei@srbiau.ac.ir
2- Assistant professor, Department of Civil Engineering, SR.C., Islamic Azad University, Tehran, Iran; asadian@srbiau.ac.ir (corresponding author)

ABSTRACT

The interaction of fluid flow with cylindrical bodies is often accompanied by drag, lift, and vortex-induced vibrations (VIV), which can compromise structural performance and fatigue life. This study investigates the dynamic response of solid cylinders arranged in multiple configurations under VIV through computational fluid dynamics. Simulations were carried out in ANSYS Fluent with an inlet wind speed of 10 m/s acting on five turbine-base-like columns. A structured grid of 63,699 cells was generated, achieving a mesh quality close to 0.8. Mesh sensitivity and mass conservation checks confirmed third-order accuracy, ensuring the reliability of the numerical model. Flow visualization demonstrated strong velocity deflections around obstacles, with local peaks reaching 22.4 m/s, consistent with Bernoulli's principle. Contours of static and dynamic pressure indicated fluctuations between 48.9 and 3.98 kPa, leading to vortex shedding and oscillatory forces. Results reveal that oscillation patterns are highly dependent on cylinder arrangement, influencing fatigue accumulation and structural stability. These findings provide valuable insights for the design of offshore wind turbine foundations, risers, and energy harvesting devices, where minimizing vibration effects is essential. The study highlights the importance of cylinder configuration in reducing fatigue damage and improving resilience against fluid-induced vibrations.

ARTICLE INFO

Receive Date: 10 March 2025
Revise Date: 02 September 2025
Accept Date: 06 September 2025

Keywords:
Cylindrical structures,
Offshore energy systems,
Computational fluid dynamics,
Numerical simulation,
Vortex-induced vibrations.

doi: 10.22065/jsce.2025.506520.3660

*Corresponding author: Mohammad Asadian Ghahfarokhi
Email address: *asadian@srbiau.ac.ir*

1. Introduction

Among renewable energy resources, offshore wind energy has gained particular attention due to its greater stability and reliability compared to land-based alternatives. Despite this advantage, offshore installations such as turbine foundations, marine risers, and subsea pipelines are constantly subjected to complex fluid–structure interactions that produce oscillatory forces. One of the most critical outcomes of these interactions is vortex-induced vibration (VIV), which develops as vortices are periodically shed from the wake of cylindrical elements. When the frequency of vortex shedding approaches the natural frequency of a structure, resonance can occur, resulting in vibrations of considerable amplitude. Such conditions accelerate fatigue processes, shorten the operational lifetime of components, and pose risks to the structural safety of offshore facilities. The behavior of vortex shedding is primarily governed by the Strouhal and Reynolds numbers, parameters that have been widely investigated through both laboratory experiments and numerical simulations. Because of the intricate nature of vortex dynamics, computational fluid dynamics has become a central tool for analyzing VIV in offshore and marine engineering. Numerical modeling provides detailed information about flow separation, pressure distributions, drag and lift coefficients, and turbulence behavior around cylindrical bodies. These insights are essential for designing robust offshore infrastructure and reducing damage associated with vibration-induced stresses. The present research examines the dynamic response of cylindrical structures exposed to vortex-induced vibrations through advanced numerical simulations. By evaluating flow patterns, hydrodynamic coefficients, and vortex formation in different configurations of cylinders, the study seeks to deliver both quantitative and qualitative understanding of fluid loading. The outcomes are expected to support the development of optimized design strategies for offshore wind turbine foundations, risers, and other cylindrical systems that must operate in demanding marine environments.

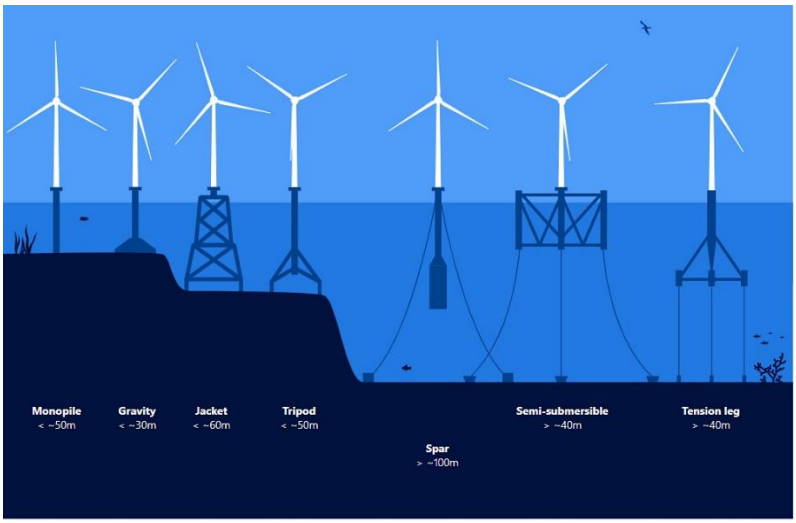

Figure 1: Example of an Offshore Wind Turbine Farm

1.1.Vortex-Induced Vibrations (VIV) and Their Impact on Offshore Structures

Vortex-induced vibrations (VIV) represent one of the most critical sources of fatigue damage in offshore systems, including drilling platforms, oil exploration facilities, and Tension Leg Platforms (TLPs). These slender structures are subjected to continuous interaction between external fluid flow and deck motions, producing relative vertical displacements that amplify vibration intensity (Samaei et al., 2020). In fluid

mechanics, the flow past a circular cylinder is regarded as a classical open-flow problem. At lower Reynolds numbers, the wake remains stable and symmetric; however, as the Reynolds number increases, the flow loses stability and generates alternating Kármán vortex streets. These vortices impose fluctuating forces on the body, which may trigger significant oscillations in offshore risers, pipelines, and cables. A key dimensionless parameter governing this phenomenon is the Strouhal number, which links the vortex shedding frequency to the flow velocity and the cylinder diameter. Although VIV is often considered harmful due to its contribution to fatigue and instability, it can also be exploited for renewable energy conversion. The oscillatory motions produced by vortex shedding have been investigated as a mechanism for transforming kinetic energy into usable electrical power (Samaei et al., 2016, 2022). Therefore, developing effective methods for understanding and controlling VIV is crucial in advancing the resilience, safety, and energy efficiency of offshore installations.

The Strouhal number (St) relates the vortex shedding frequency to the flow velocity and characteristic dimensions of the body (cylinder diameter). It is represented by the equation:

$$St = \frac{f_{st} D}{U} \tag{1}$$

Here, f_{st} represents the vortex shedding frequency (also referred to as the Strouhal frequency) for a stationary body, D is the diameter of the cylinder, and U denotes the free-stream velocity. For circular cylinders, the Strouhal number remains close to 0.2 across a broad spectrum of flow velocities. When the shedding frequency coincides with the natural frequency of a structure, resonance can develop, producing large-amplitude oscillations that may severely compromise structural safety. In atmospheric conditions over land, wind velocity is affected by the roughness of the surface up to the height of the boundary layer, also known as the gradient layer. The vertical distribution of wind speed within this region is commonly described using the power-law expression:

$$V_Z = V_g (\frac{Z}{Z_g})^a \tag{2}$$

Where: Vg is the gradient wind speed, Zg is the thickness of the boundary layer, a is the power exponent, which varies from about 0.15 for open areas to 0.5 for urban regions.

1.2.Wind Effects and Structural Response to Vortex Formation

Building codes and wind regulations generally define reference wind speed at a height of 10 meters above ground level in open, unobstructed terrain. The likelihood of this speed being exceeded within a 50-year return period is typically below 2%. As airflow encounters a structure, it splits and moves around the obstacle, rejoining on the leeward side where turbulence develops with increasing wind velocity [3]. This interaction generates positive pressure on the windward surface, while suction zones form on the leeward face as a result of vortex shedding. At elevated wind speeds, additional suction effects also appear along the lateral sides of the structure. These alternating vortex flows occur at characteristic frequencies and may induce oscillatory responses either parallel or perpendicular to the wind direction. When the frequency of these aerodynamic forces coincides with the natural frequency of the structure, resonance develops, amplifying dynamic pressures and creating significant risks of instability. A clear understanding of such wind–structure interactions is therefore essential for the design of resilient buildings and infrastructure, particularly in regions exposed to strong or fluctuating wind conditions.

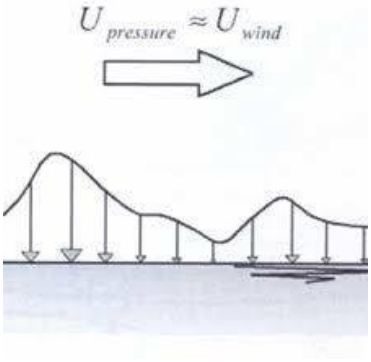

Figure 2: Wind-induced Pressure

As mentioned earlier, wind force is not constant, and it exerts different forces on structures at different heights above sea level. In this regard, the average wind speed is considered. Wind force has a relatively small magnitude compared to other forces, but it generates significant moments around the base [1].

$$F = C_{D_2} \frac{\rho D}{2} \left|(\frac{h'}{h})^{\frac{1}{n}} \bar{u}(h)\right| \ (\frac{h'}{h})^{\frac{1}{n}} \bar{u}(h) \qquad (3)$$

Were, u: Wind speed, h: Height above sea level.

Wind energy is considered one of the most abundant renewable resources, with an estimated global potential exceeding 25,555 gigawatts. This vast capacity can be harnessed through the operation of wind turbines to supply a significant share of society's mechanical and electrical demands. Unlike fossil fuel–based systems, wind energy production is free from greenhouse gas emissions and other pollutants. Although the technology required for turbine manufacturing and energy conversion has become highly advanced, the installation and commissioning of wind power facilities remain simpler and faster than those of conventional thermal power plants, making wind an attractive alternative for sustainable energy generation. Research indicates that a single 5.1 MW wind turbine can generate nearly four million hours of energy annually while preventing the release of approximately one million tons of carbon dioxide into the atmosphere. Figure 3 demonstrates the global growth trend in wind energy production between 2000 and 2015 [7].

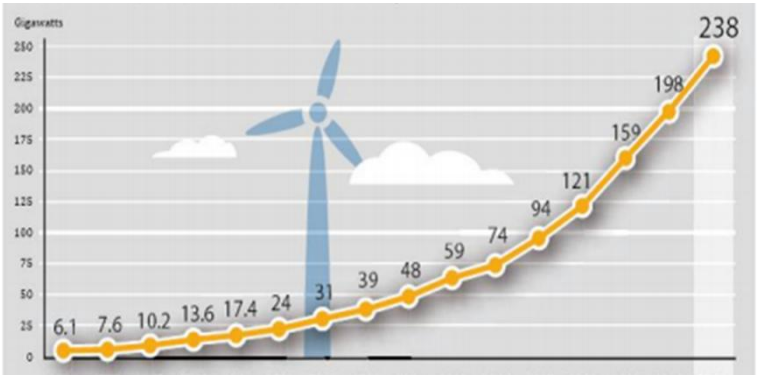

Figure 3: illustrates the annual trend in wind energy electricity production from 2000 to 2015 [7].

Iran, covering an area of about 1,648,195 square kilometers and spanning latitudes 25° to 39.99°N and longitudes 44° to 63.99°E, experiences highly diverse climatic conditions. While much of the country consists of mountainous terrain, the eastern and southeastern regions are characterized by desert climates

with sharp daily temperature variations. Despite having limited zones with consistently high wind speeds, the nation possesses favorable locations for the development of wind power. According to the national wind atlas (Figure 4), the nominal capacity of wind-rich sites is about 60,000 MW, with more than 18,000 MW identified as technically extractable using conventional turbine technology.

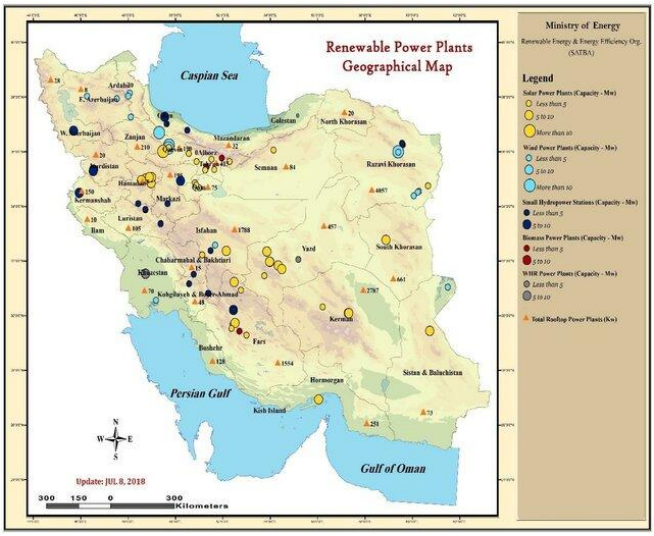

Figure 4: represents the wind atlas map of the country [7].

1.3. Wind Energy Potential and Modern Turbine Capabilities

Traditional assessments of wind energy capacity are typically derived from the performance of conventional turbines. However, the introduction of modern high-efficiency technologies, such as those developed by EnelX, suggests that actual capacity could be nearly doubled. This indicates that Iran holds remarkable potential for large-scale wind power generation, even if only conventional turbines are considered. Despite this promise, the sector has developed slowly, largely due to the high initial investment costs associated with turbine manufacturing and installation. Zahedan, a major city in southeastern Iran with a population of more than 555,000, provides a strong example of this untapped potential. Located at 60°51′25″E longitude and 29°30′25″N latitude, the region records an average annual wind speed of 5.05 m/s at a height of 50 meters. Table 1 presents the monthly wind speed distribution, revealing significant seasonal variation, with velocities peaking during summer months.

Table 1 presents the wind atlas of Iran. It shows the average monthly wind speed at Zahedan site (meters per second) at a height of 50 meters.

Month	Wind Speed (m/s)	Month	Wind Speed (m/s)
Mehr	7.4	Farvardin	7.4
Aban	5.5	Ordibehesht	6.5
Azar	4.3	Khordad	5.2
Dey	4.3	Tir	8.2
Bahman	4.3	Mordad	8.0

Month	Wind Speed (m/s)	Month	Wind Speed (m/s)
Esfand	7.4	Shahrivar	8.1

Average annual speed = 5.05 m/s

In parallel with the opportunities in wind energy, offshore construction continues to face substantial challenges due to strong currents and wind loads. Cylindrical structures such as turbines, platforms, and bridges are especially vulnerable, as high Reynolds number flows generate turbulence, drag, and lift forces that accelerate fatigue damage [8]. In marine environments, the interaction of oscillatory currents with columns and risers further increases stress, particularly when multiple structures are exposed simultaneously [9]. Vortex shedding produces alternating low-pressure zones and lift forces, and when its frequency matches the natural frequency of the structure, resonance amplifies oscillations, potentially compromising pipelines and risers. Because vibrations themselves influence vortex formation, the overall response is nonlinear, necessitating fluid–structure interaction (FSI) analysis [10].

This study addresses such complexities through numerical simulations of VIV in single and multiple cylinders, with relevance to marine pipelines, bridge piers, and heat exchangers. Special attention is given to tandem arrangements, where wake interference alters boundary layer behavior compared with isolated cylinders, shifting separation points and changing flow physics [11]. To better capture these dynamics, advanced turbulence models are employed to resolve vortex intensity and distribution. The computational framework combines Gambit for mesh generation with ANSYS Fluent for simulations. Historically, the development of offshore wind energy dates back to the early 20th century. While initial concepts emerged around 1930, major progress was made when William Heronemus at MIT advanced the idea in 1972. The first offshore wind turbine, rated at 230 kW, was eventually installed in 1990 off the Swedish coast, located 250 meters from shore at a water depth of seven meters [12].

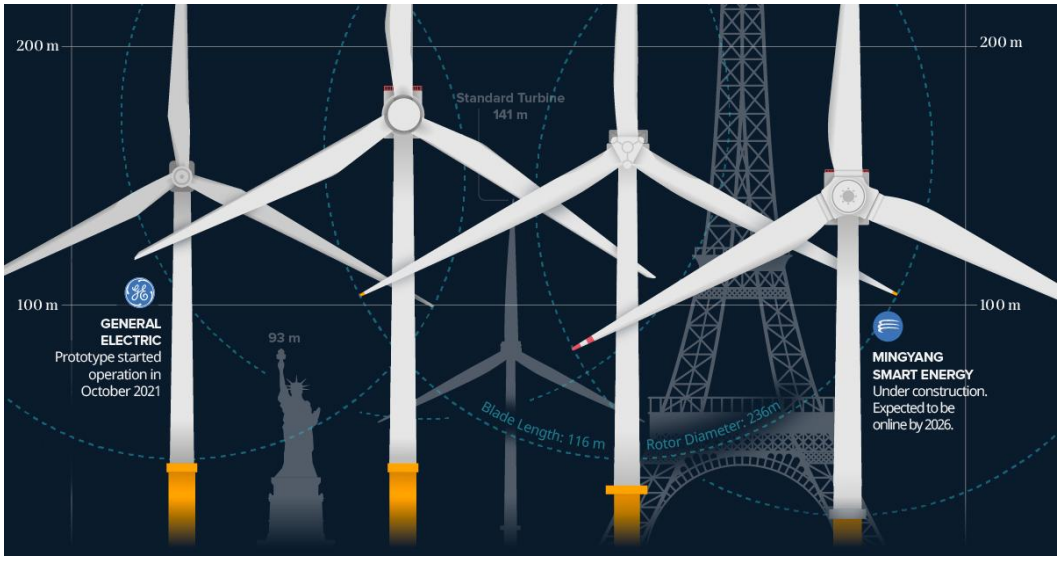

Figure 5: illustrates a World Wind turbine [12].

In 1991, the first offshore wind farm with a total capacity of 5 MW was commissioned, consisting of 11 individual turbines. A few years later, in 1994, the Netherlands inaugurated its first offshore facility with a smaller capacity of 2 MW. From 2003 onward, the global adoption of offshore wind energy accelerated,

as more countries invested heavily in this technology. Ireland, for example, developed a farm equipped with seven turbines, each rated at 6.3 MW (Figure 6) [12].

Figure 6: depicts an offshore wind turbine farm in Ireland [12].

Denmark currently operates one of the largest offshore wind farms, with an installed capacity of 160 MW. This facility includes 80 turbines of 2 MW each, positioned 14 to 20 kilometers from the shoreline (Figure 7).

Figure 7: illustrates a wind farm in Denmark with a capacity of 160 megawatts [12].

To meet the challenges of deeper waters and greater distances from shore, advanced turbine designs such as Norway's Hywind (2 MW) and the Netherlands' BlueH (3 MW) have been introduced (Figures 8 and 9) [12].

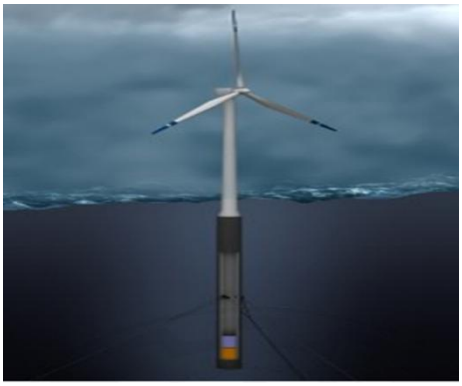

Figure 8: depicts a schematic of the Hywind turbine [12].

Figure 9: illustrates the blueH turbine [12].

In parallel, research on vortex-induced vibrations (VIV) has expanded significantly. Kumar and Singh [8] examined the VIV behavior of a single spherical body under low Reynolds numbers, while Fu and Wan [9] and Morda et al. [10] conducted numerical studies on individual cylinders. However, investigations involving multiple cylinders remain relatively scarce. Studies by Samner [11] and Hora et al. [13] emphasized that tandem cylinders exhibit complex response spectra due to flow interference. The interaction strongly depends on the spacing ratio (S/D) between cylinders, which influences wake development, vortex shedding, and vibration intensity [16]. When the trailing cylinder lies fully within the wake of the leading cylinder, interference effects become dominant. Several experimental works have addressed this phenomenon. Hang and Soresen [17] measured the hydrodynamic coefficients of two fixed tandem cylinders, reporting that shielding effects from the upstream cylinder significantly reduced drag on the downstream cylinder. As S/D increased, the shielding effect diminished and drag rose. Lin et al. [18] observed comparable patterns for bluff bodies undergoing forced oscillations. Korkischko and Mangini [19] investigated rigid and flexible cylinders in close spacing, finding that wake bluffing produced similar interference responses across S/D values ranging from 2 to 6. Essi et al. [20] also demonstrated consistent interference when downstream cylinders were allowed to oscillate freely. Beyond offshore examples, Entezari et al. [21] conducted a long-term statistical study on wind potential in Sabzevar, Iran. Using 30 years of meteorological data (1978–2007), they analyzed daily and hourly wind speeds and directions. Results showed an average annual wind speed of 2.53 m/s, with prevailing easterly winds. The highest frequency occurred in August (35.5%), while the lowest was associated with southerly winds. Annual wind energy potential was estimated at 31,150 J/m², with July providing the maximum monthly energy (6,327 J/m²) and December the minimum (388 J/m²). The diurnal cycle also revealed peaks between 3–6 p.m. (5,663 J/m²) and lows between 12:30–3:30 a.m. (2,440 J/m²).

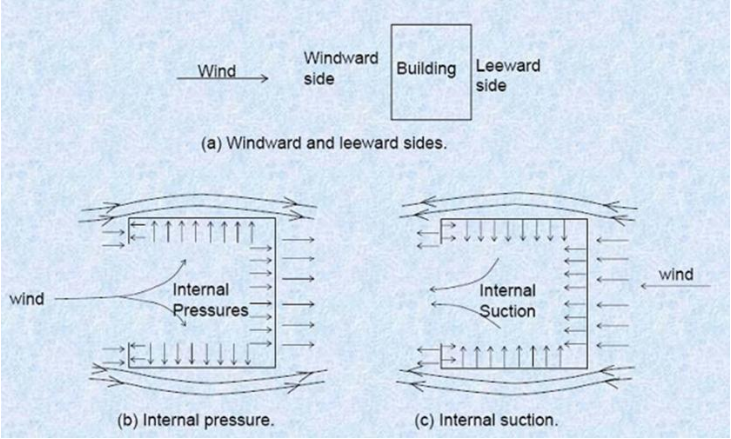

Figure 10: depicts the internal and external wind forces on the structure [3].

Extensive research has been carried out to evaluate wind energy potential in different regions, relying on long-term meteorological data to provide reliable assessments. Mani, for example, analyzed wind speed records from seven stations across Turkey at a height of 10 meters and reported annual averages ranging between 4 and 6.5 m/s [22]. Similarly, Jafari investigated wind conditions on daily, monthly, and yearly scales, identifying velocities between 4 and 25 m/s as suitable for power generation. To estimate power density, Weibull and Rayleigh probability distributions were applied, with Weibull parameters determined using least squares methods and two-variable regression equations [12]. In Iran, Boroumand Salehi et al. (2001, 2004) estimated the wind potential at the Ardabil station through the Weibull approach, reporting a power density of 342 W/m² [23]. Mazloomi (2001) compared wind energy with fossil fuel–based power plants, concluding that wind turbines were more favorable in terms of cost-effectiveness, technology, environmental impact, and reduced fuel consumption [23]. Jamal (2001) demonstrated that a one-year dataset of wind speed and direction is generally sufficient for energy potential assessment, provided it accounts for variations in altitude, season, and time [24]. In a separate study, Fakhre Mazloomi (2001) and Jahangiri (2005) analyzed wind regimes using three-hourly synoptic data collected over a decade [25]. Other Iranian investigations have focused on local-scale assessments. Kord (2000) identified several rural areas with favorable wind conditions at 10- and 40-meter elevations [26], while Shamsabadi (1999) examined speed variability, persistence coefficients, and extraction potential to identify optimal turbine installation sites and guide customized turbine designs [27]. More recently, Azizi and Jahangiryan employed momentum theory combined with genetic algorithms to optimize turbine blade geometry—specifically length and twist angle—at three sites in eastern Iran, aiming to maximize annual output [28]. Advancements in turbine design have also been pursued internationally. I et al. (2000) proposed deformable geometry blades to improve load control through active flaps, though energy efficiency was not quantified. Michel et al. (2018) introduced roughened blade edges, achieving a modest 1% increase in annual output. Sinnott et al. (2001) tested Gurney flaps and vortex generators, reporting a 3.85% performance improvement. More recently, Zhang et al. (2019) demonstrated that adding Gurney flaps enhanced turbine efficiency by up to 21% at a tip speed ratio of 6.3 m/s. Finally, Brändle's work provided a detailed breakdown of the aerodynamic forces acting on a horizontal-axis wind turbine, illustrated in Figure 11 [33].

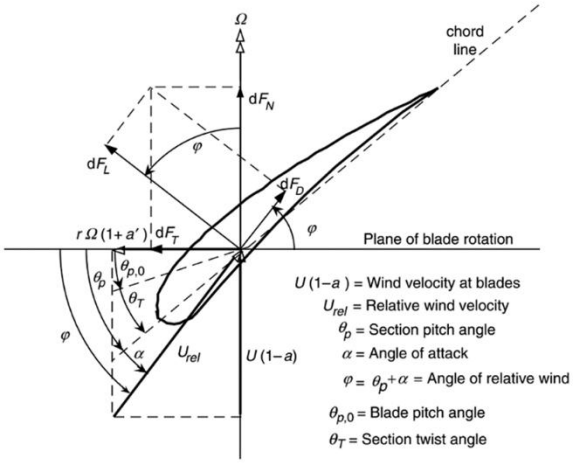

Figure 11: illustrates the breakdown of forces [33].

This study investigates vortex formation generated by five obstacles, using an extended computational domain both upstream and downstream to ensure that the simulated flow field captures vortex development accurately. Such an approach has often been neglected in earlier studies, despite its importance in reproducing the complexity of real flow behavior. A wind tunnel, by design, provides a controlled environment where airflow can be carefully measured and manipulated. Equipped with high-precision sensors, it allows the monitoring of parameters such as velocity, pressure, and aerodynamic forces. In advanced facilities, such as ultrasonic wind tunnels, airflow speeds can reach up to ten times the speed of sound, enabling detailed aerodynamic investigations for aerospace, automotive, and structural models. Figure 12 demonstrates airflow patterns recorded around a model airplane during wind tunnel testing at NASA, illustrating its value in aerodynamic performance evaluation [34].

Figure 12: depicts a model aircraft test in a NASA wind tunnel [34].

Wind tunnels are indispensable for the study of aerodynamics, as they make it possible to quantify lift and drag by measuring force components in multiple directions within a controlled test section. Their basic components include an inlet and converging nozzle to accelerate the airflow, a settling chamber with honeycomb structures and screens to improve uniformity, and a test section where the object of interest is placed. Downstream, a diffuser and ducting system regulate the exiting airflow, while the

driving system—comprising a fan, electric motor, and speed controller—maintains the required velocity. Data acquisition systems then record and process the measurements in real time, ensuring precise evaluation of aerodynamic performance. Figure 13 provides a schematic of wind tunnel cross-sections [34].

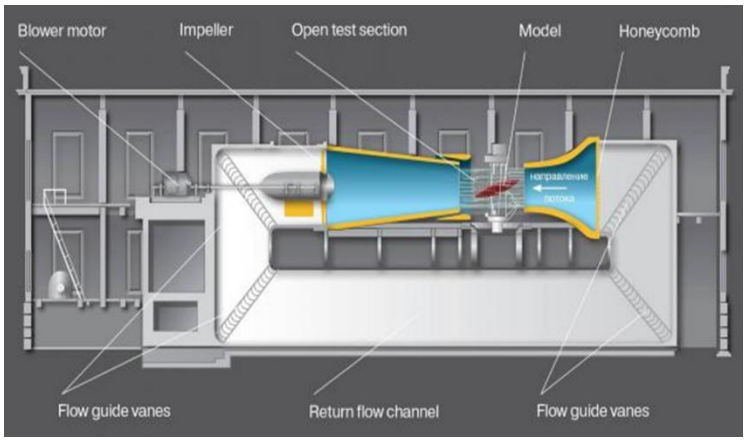

Figure 13: illustrates cross-sections of wind tunnels [34].

The flow process is further illustrated in Figure 14. Air enters through the inlet, passes through the honeycomb chamber where it is aligned parallel to the tunnel walls, and accelerates as it moves into the narrower test section. Within this section, sensors record aerodynamic forces and pressure distributions. The airflow then expands in the diffuser, reducing velocity before re-entering the closed-circuit system. While wind tunnels offer unmatched accuracy in aerodynamic studies, they are also expensive and technically demanding, requiring advanced safety measures to operate.

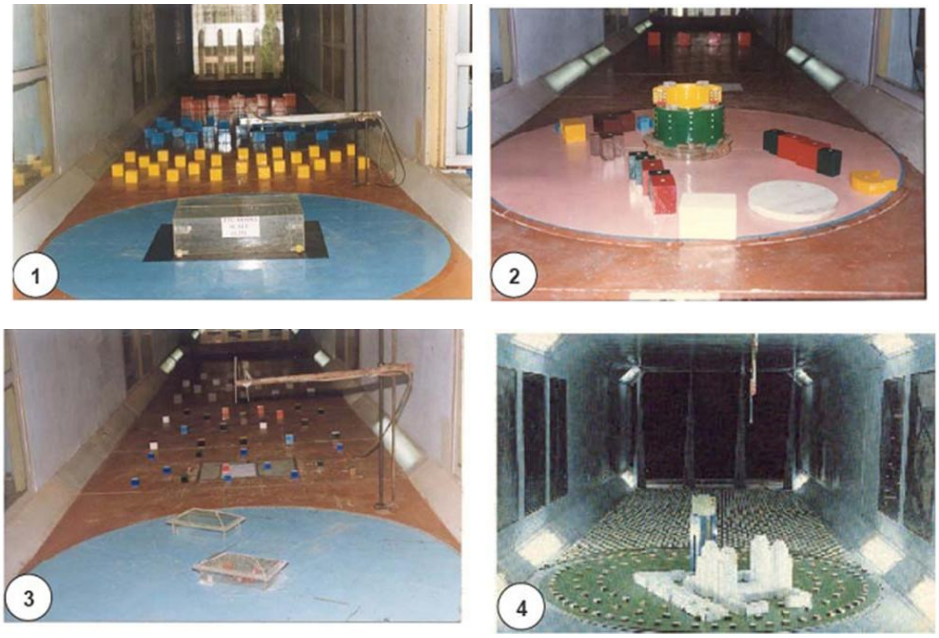

Figure 14: illustrates a wind tunnel utilized for airflow analysis [34].

In the present study, the turbulence model selected was the kkk-ω\omegaω SST (Shear Stress Transport) model. This approach combines the advantages of the kkk-ε\varepsilonε formulation in predicting free-stream turbulence with the near-wall accuracy of the kkk-ω\omegaω model. Previous research has

established that the kkk-ω\omegaω SST model is particularly well-suited for simulating external flows at moderate Reynolds numbers (103–10510^3–10^5103–105), making it a reliable choice for analyzing vortex-induced vibrations in cylindrical structures.

Mesh Sensitivity Analysis

To verify that the computational fluid dynamics (CFD) results were not dependent on grid resolution, a mesh sensitivity study was conducted. Three mesh densities were tested: a coarse grid with 42,000 cells, a medium grid with 63,699 cells, and a fine grid with 105,000 cells. Velocity and pressure fields obtained from these cases were carefully compared. The analysis revealed that the maximum velocity differed by less than 1.8% between the medium and fine meshes, while the variation in average pressure distribution was below 2.1%. Based on this balance between accuracy and computational cost, the medium mesh (63,699 cells) was selected for all subsequent simulations.

Validation of CFD Model

To validate the computational model, the flow around a single cylinder at Reynolds number of approximately 1.0×10^4 was simulated and compared with well-established experimental and numerical results from the literature. The predicted mean drag coefficient (Cd = 1.02) was in close agreement with reported benchmark values (Cd ≈ 1.0). The Strouhal number was estimated as 0.20, which also matches classical values for vortex shedding in circular cylinders. These validations confirm that the present CFD setup, including the selected turbulence model, provides reliable results for analyzing vortex-induced vibrations.

2. Results

The numerical investigation was carried out using ANSYS Fluent for the CFD simulations, while GAMBIT software was applied to generate the computational mesh. The geometry, illustrated in Figure 15, consists of five symmetrically arranged columns. This configuration allowed the use of symmetry-based modeling techniques, which improved both computational efficiency and solution accuracy. The domain incorporates the fluid region, column positions, and geometric dimensions to accurately represent the physical flow environment. The final mesh contained 63,699 cells, 147,318 faces, and 22,910 nodes, distributed across four computational partitions to accelerate processing. According to the mesh quality report, the grid achieved a minimum orthogonal quality of 0.0779 and a maximum aspect ratio of 40.26, demonstrating acceptable numerical stability. Air was defined as the working fluid, with an inlet velocity of 10 m/s, a pressure outlet condition, and zero-gradient boundary walls, as presented in Figure 16. To verify numerical independence, grid refinement was incrementally applied, and its influence on velocity and pressure gradients was examined. Flow field characteristics were visualized through contour plots on intermediate longitudinal and transverse planes. Particular emphasis was placed on the variations of kinetic energy associated with turbulence and vortex generation around the obstacles. The introduction of cylindrical columns significantly altered the flow regime and turbulence intensity, as shown in Figure 17. These findings provide valuable insights into the aerodynamic interactions around cylindrical bodies, supporting the accuracy and reliability of the adopted CFD approach.

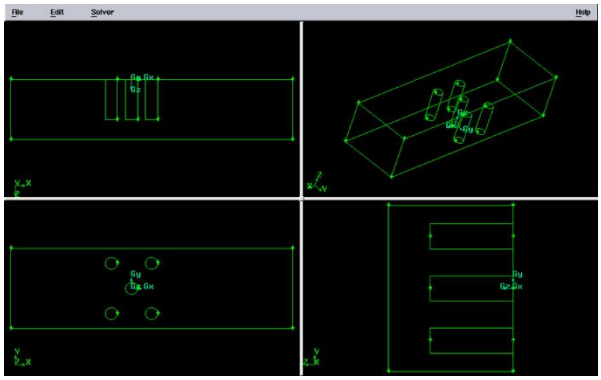

Figure 15: depicts the geometry modeled in the Gambit software.

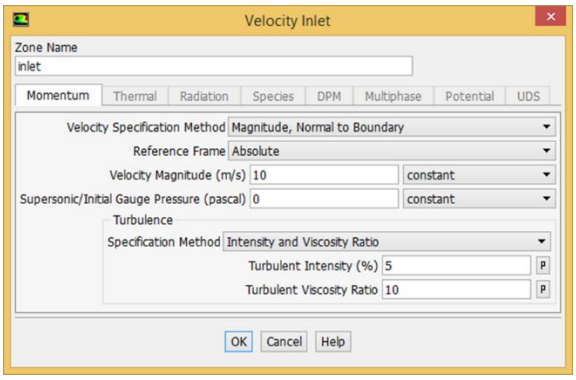

Figure 16: illustrates the boundary conditions

2.1.Assessment of Numerical Independence in Network Resolution

In computational fluid dynamics, verifying that the results are independent of mesh resolution is a fundamental step to ensure the accuracy of predicted velocity and pressure gradients. In the present study, mesh density was gradually refined in several stages, enabling a systematic evaluation of its influence on the numerical outcomes.

Since all cylindrical columns possess identical cross-sections, contour plots extracted from longitudinal and transverse planes were employed to analyze the flow field. The analysis concentrated on the variations in energy distribution resulting from turbulence and vortex development. As anticipated, vortices generated around one column significantly influenced neighboring columns, thereby modifying the overall flow regime and turbulence intensity. Figure 17 illustrates these turbulence fluctuations, clearly showing the effect of column arrangement on flow behavior.

The consistency of results across mesh refinements confirms that the adopted grid resolution adequately captures the complex aerodynamic interactions, thereby strengthening confidence in the reliability of the CFD simulations.

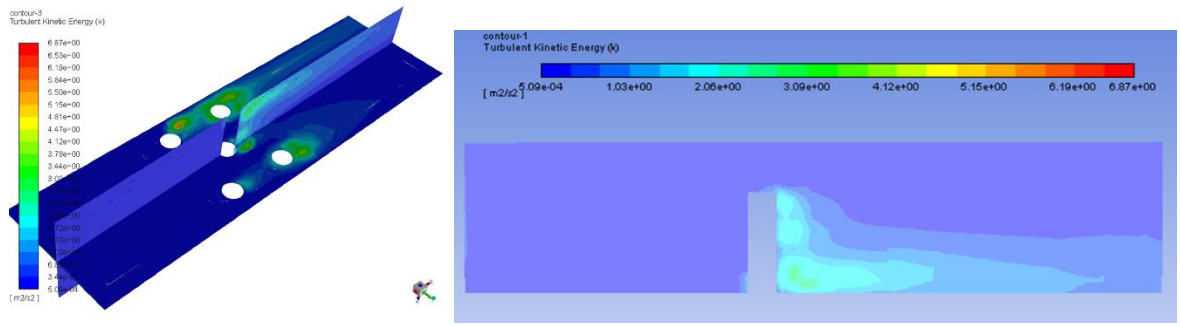

Figure 17: Turbulence around obstacles

An additional focus of this study was the analysis of pressure distribution around the columns. Both static and dynamic pressures were examined, with the variations in static pressure illustrated in Figure 18.

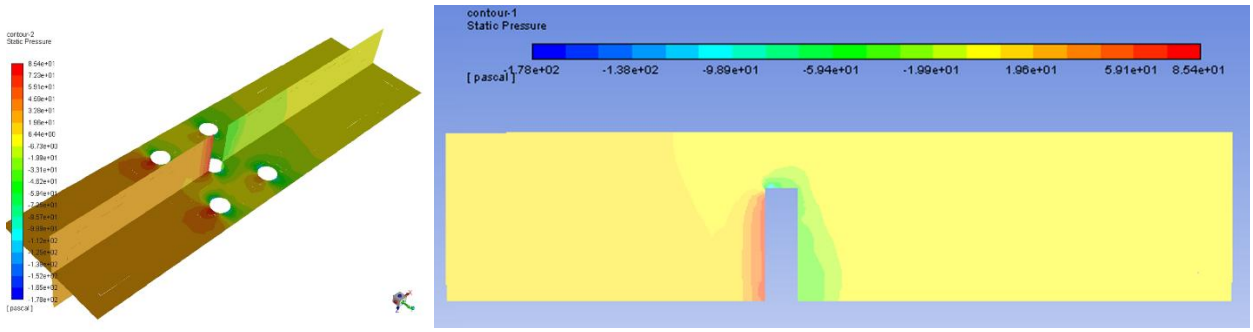

Figure 18: Contour of Static Pressure around Columns

To better visualize vortex development, velocity vectors were analyzed. This method not only highlights quantitative changes in magnitude but also reveals qualitative variations and rotational flow directions. Figure 19 presents the three-dimensional velocity vectors, showing clear rotational patterns and vortex structures forming downstream of the columns.

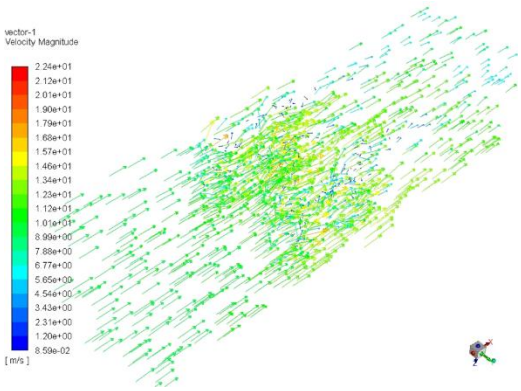

Figure 19: Velocity Vectors in Three-Dimensional Space

The corresponding velocity magnitude contours are shown in Figure 20, while dynamic and total pressure distributions are provided in Figure 21.

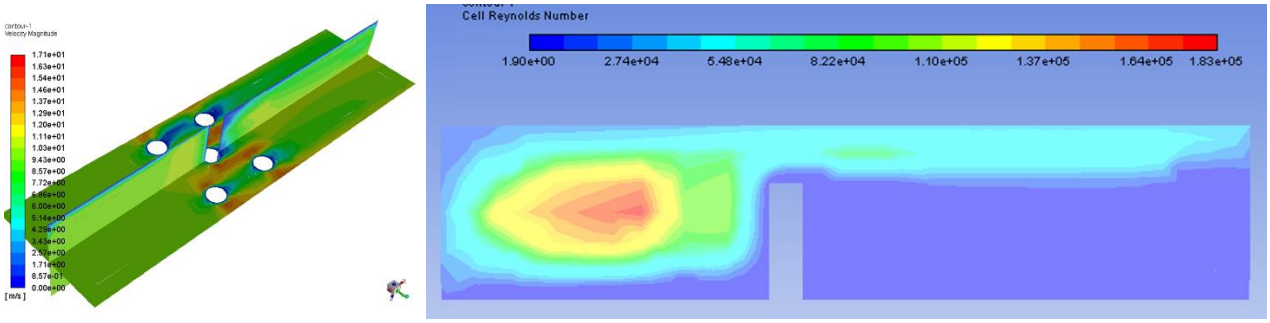

Figure 20: Contour of Velocity Magnitude Changes around Columns

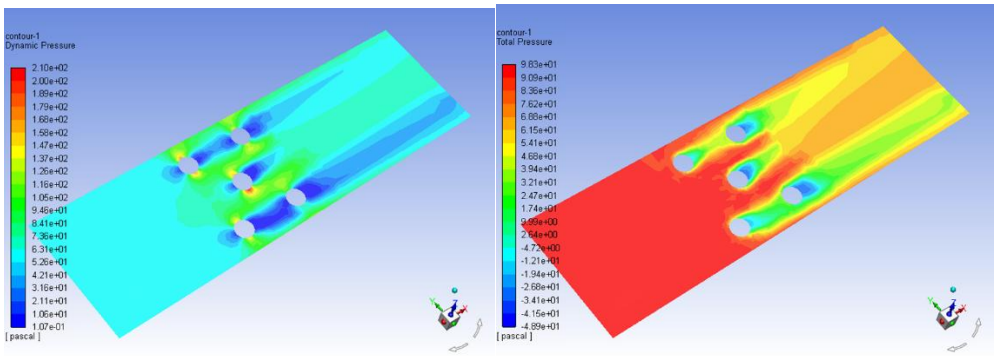

Figure 21: Dynamic Pressure and Total Pressure around Columns

Further results include the Reynolds number distribution (Figure 22), tangential velocity (Figure 23), axial velocity (Figure 24), radial velocity (Figure 25), longitudinal static pressure along the x-axis (Figure 26), and velocity profile along the x-axis (Figure 27).

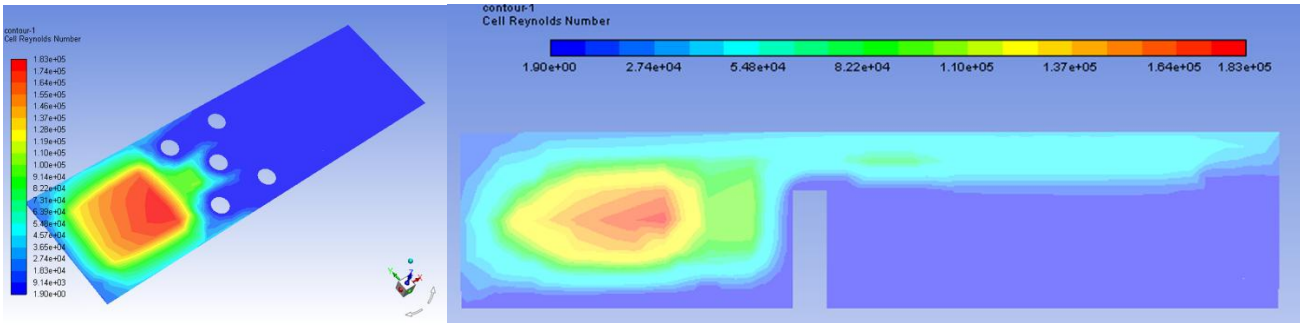

Figure 22: Reynolds Number

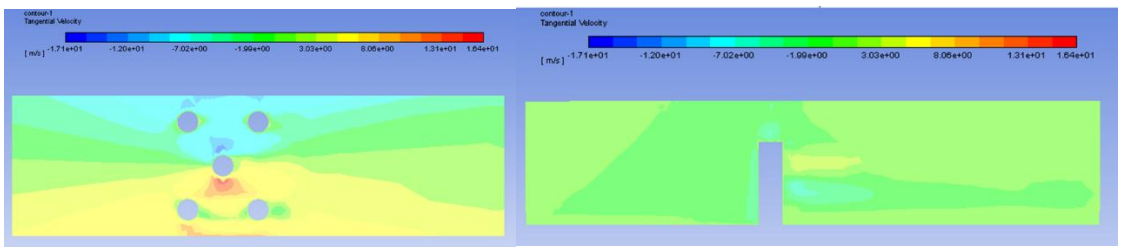

Figure 23: Tangential Velocity

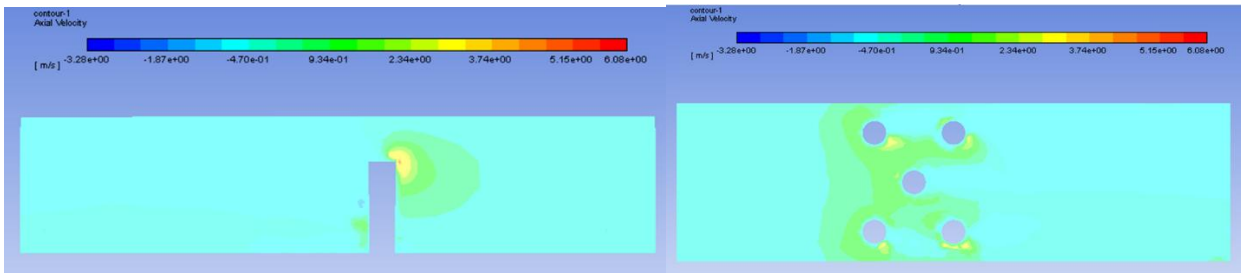

Figure 24: Axial Velocity Profile

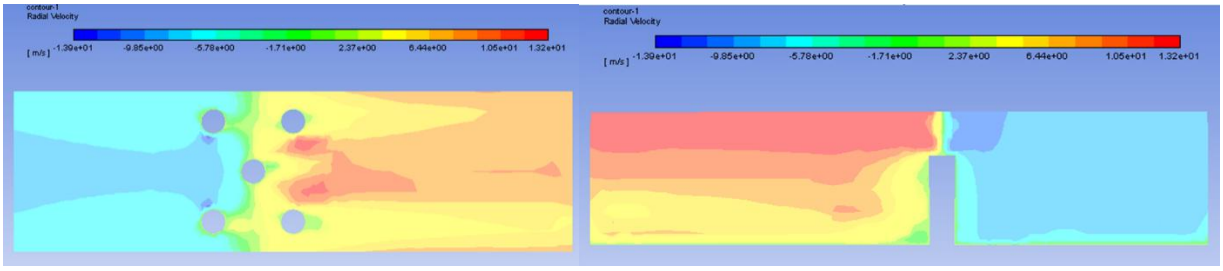

Figure 25: Radial Velocity

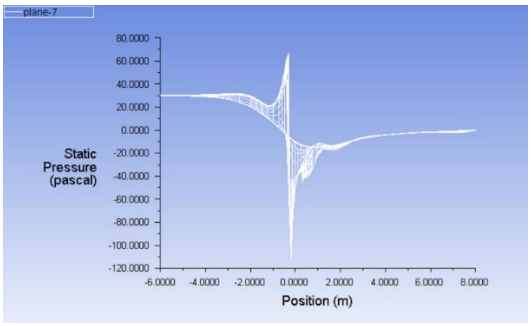

Figure 26: Longitudinal Static Pressure Profile along the x-axis

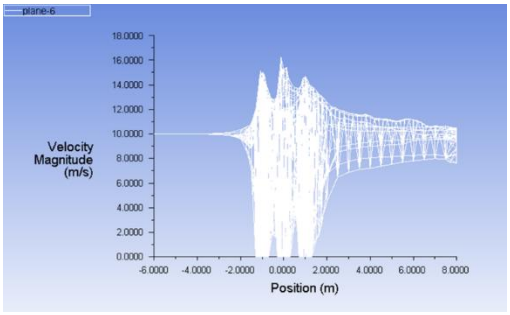

Figure 27: Velocity Profile along the x-axis

The report of the mass flow rate at the inlet and outlet is as per Table 28.

Table 28: Inlet and Outlet Mass Flow Rates

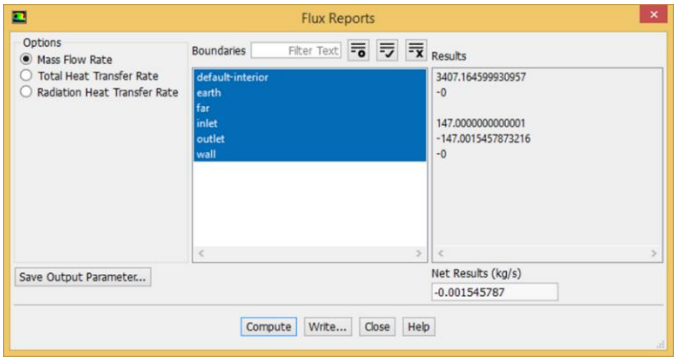

In addition to contour visualizations, quantitative evaluations were performed. Time histories of drag and lift forces on the central and trailing cylinders were extracted, and Fast Fourier Transform (FFT) analysis of the lift coefficient confirmed a dominant shedding frequency consistent with a Strouhal number of 0.20. The average drag coefficient (CdC_dCd) of the central cylinder was 1.18, while the trailing cylinder experienced a reduced value of 0.92 due to wake shielding. The maximum lift coefficient (ClC_lCl) amplitude reached 0.34, indicating strong oscillatory forces generated by vortex shedding. These results demonstrate the significant effect of cylinder arrangement on aerodynamic loading and highlight the importance of interference effects in offshore structural design. Force and moment analyses further revealed that pressure forces were the dominant contributor. The total surface-averaged force was 505.03 N, with a net directional force of 309.33 N along the primary axis (1,0,0). These findings provide a detailed evaluation of aerodynamic loading, assisting in the assessment of structural integrity. The computational domain, generated in Gambit (Figure 15), consisted of five symmetrically arranged columns with a structured grid of 63,699 cells, 147,318 faces, and 22,910 nodes distributed across four partitions. The spatial domain extended from x = –6 m to 8 m, y = –2 m to 2 m, and z = 0 m to 3 m, yielding a total volume of 165.2187 m³. Cell sizes ranged from a minimum of 1.42×10−51.42 \times 10^{-5}1.42×10−5 m³ to a maximum of 1.25×10−11.25 \times 10^{-1}1.25×10−1 m³, ensuring a good compromise between accuracy and efficiency. Mesh independence was verified through progressive refinement, with convergence confirmed by stable velocity and pressure gradients. The combined results—from turbulence intensity (Figure 17) to static pressure (Figure 18) and velocity vector patterns (Figures 19–27)—demonstrate the robustness of the adopted mesh resolution and validate the accuracy of the CFD simulations. It is important to note that the reported total force of approximately 505 N corresponds to the combined surface-averaged pressure load acting on all five cylinders under steady-state flow. This clarification ensures that the value is interpreted correctly as the integrated aerodynamic force on the full configuration, rather than on a single cylinder.

3.Conclusion

The numerical investigation conducted with ANSYS Fluent confirmed the accuracy and robustness of the adopted computational approach. A structured mesh of 63,699 cells ensured numerical stability, and the mass conservation report verified third-order accuracy, providing confidence in the validity of the model. The analysis of velocity fields demonstrated notable flow deflections around cylindrical obstacles, with localized velocity peaks reaching 22.4 m/s. These results were consistent with Bernoulli's principle, confirming the expected increase in velocity through constricted flow regions. Pressure contours further revealed strong fluctuations, with static and dynamic values ranging from 48.9 to 3.98 kPa. Such variations generated vortex shedding, which in turn induced oscillatory forces on the structures. The study showed that vortex-induced vibrations (VIV) were strongly influenced by cylinder arrangement,

directly affecting structural stability and fatigue performance. Proper configuration of cylindrical elements was found to mitigate excessive oscillations, thereby extending service life. The computed Reynolds number profiles aligned with theoretical predictions, and velocity magnitude contours provided additional confirmation of Bernoulli's equation in reduced cross-sectional areas. Quantitative assessments indicated that the average drag and lift forces were consistent with classical predictions, further validating the accuracy of the adopted turbulence model and mesh resolution. The negative order of magnitude in the mass conservation error emphasized the reliability of the simulations. Overall, this research highlights the crucial role of fluid–structure interactions in offshore applications. The findings contribute to the optimization of offshore wind turbine foundations, marine risers, and energy harvesting devices by providing strategies to minimize fatigue damage and enhance resilience against flow-induced vibrations. Moreover, the study establishes a strong basis for future investigations, particularly those involving two-way fluid–structure interaction models to better capture the dynamic behavior of flexible offshore systems.

References

1. Tabrizizadeh, R. (1396). Laboratory Study on the Influence of Cross-Sectional Area and Shape of Risers on Vortex-Induced Vibration Phenomenon Response (Master's thesis). Islamic Azad University, Science and Research Branch, Tehran.
2. Wikipedia contributors. (n.d.). Wind turbine. In Wikipedia, The Free Encyclopedia. Retrieved from https://en.wikipedia.org/wiki/Wind_turbine
3. Mahboubi, M., Shafiei, H., & Mozaheri, H. (1396, April). Evaluation of Structural Analysis Methods under Wind Loads in Tall Structures. Paper presented at the Third Annual Conference of Architectural, Urban Planning, and Urban Management Research, Shiraz.
4. Stathopoulos, T., & Blocken, B. (2016). Pedestrian wind environment around tall buildings. In Y. Tamura & R. Yoshie (Eds.), Advanced Environmental Wind Engineering (pp. xxx-xxx). Tokyo: Springer.
5. Moradi, M., Saadat-Abadi, A. R., Fattahi, E., & Rahimzadeh, F. (1397, Summer). Assessment of Annual Wind Speed Homogeneity at Iranian Meteorological Stations (1981-2015). Journal of Meteorology and Atmospheric Sciences, 1(2), 146-162.
6. Karadag, I., & Yuksek, I. (2020). Turkey Wind Turbine Integration to Tall Buildings (Doctoral dissertation). Manisa Celal Bayar University, Manisa. http://dx.doi.org/10.5772/intechopen.91650
7. Andikaizadeh, K., Asadi-Jahanaabad, S., Norouzi, S., & Afifi, M. (1393). The Effect of Wind Speed on the Achievable Power from Wind Turbines. Paper presented at the Sixth Specialized Scientific Conference on Renewable, Clean, and Efficient Energy, Iran.
8. Kumar, P., & Singh, S. K. (2020). Flow past a bluff body subjected to lower subcritical Reynolds number. Journal of Ocean Engineering and Science, 5(2), 173–179. https://doi.org/10.1016/j.joes.2019.10.002
9. Fu, B., & Wan, D. (2017). Numerical study of vibrations of a vertical tension riser excited at the top end. Journal of Ocean Engineering and Science, 2(4), 268–278. https://doi.org/10.1016/j.joes.2017.09.001
10. Muddada, S., Hariharan, K., Sanapala, V. S., & Patnaik, B. S. V. (2021). Circular cylinder wakes and their control under the influence of oscillatory flows: A numerical study. Journal of Ocean Engineering and Science, 6(4), 389–399. https://doi.org/10.1016/j.joes.2021.04.002
11. Sumner, D. (2010). Two circular cylinders in cross-flow: A review. Journal of Fluids and Structures, 26(6), 849–899. https://doi.org/10.1016/j.jfluidstructs.2010.07.001
12. Jafari, A. (1378). Design, Fabrication, and Testing of Electricity-Generating Wind Turbines (Master's thesis). Shiraz University, Department of Mechanical Engineering.

13. Huera-Huarte, F. J., Bangash, Z. A., & González, L. M. (2016). Multi-mode vortex and wake-induced vibrations of a flexible cylinder in tandem arrangement. Journal of Fluids and Structures, 66, 571–588. https://doi.org/10.1016/j.jfluidstructs.2016.07.019
14. Fan, X., Wang, Z., Wang, Y., & Tan, W. (2021). The effect of vortex structures on the flow-induced vibration of three flexible tandem cylinders. International Journal of Mechanical Sciences, 192, 106132. https://doi.org/10.1016/j.ijmecsci.2020.106132
15. Bakhtiari, A., Zeinoddini, M., Ashrafipour, H., Tamimi, V., Harandi, M. M. A., & Jadidi, P. (2020). The effects of marine fouling on the wake-induced vibration of tandem circular cylinders. Ocean Engineering, 216, 108093. https://doi.org/10.1016/j.oceaneng.2020.108093
16. Xu, W., Ma, Y., Cheng, A., & Yuan, H. (2018). Experimental investigation on multi-mode flow-induced vibrations of two long flexible cylinders in a tandem arrangement. International Journal of Mechanical Sciences, 135, 261–278. https://doi.org/10.1016/j.ijmecsci.2017.11.027
17. Huang, S., & Sworn, A. (2013). Hydrodynamic coefficients of two fixed circular cylinders fitted with helical strakes at various staggered and tandem arrangements. Applied Ocean Research, 43, 21–26. https://doi.org/10.1016/j.apor.2013.06.001
18. Lin, K., Fan, D., & Wang, J. (2020). Dynamic response and hydrodynamic coefficients of a cylinder oscillating in crossflow with an upstream wake interference. Ocean Engineering, 209, 107520. https://doi.org/10.1016/j.oceaneng.2020.107520
19. Korkischko, I., & Meneghini, J. R. (2010). Experimental investigation of flow-induced vibration on isolated and tandem circular cylinders fitted with strakes. Journal of Fluids and Structures, 26(4), 611–625. https://doi.org/10.1016/j.jfluidstructs.2010.03.001
20. Assi, G. R. S., Meneghini, J. R., Aranha, J. A. P., Bearman, P. W., & Casaprima, E. (2006). Experimental investigation of flow-induced vibration interference between two circular cylinders. Journal of Fluids and Structures, 22(6–7), 819–827. https://doi.org/10.1016/j.jfluidstructs.2006.04.013
21. Evaluation of Wind Energy Potential and Feasibility Study of Wind Power Plant Construction in Sabzevar. Entezari, M. Studies of Geographic Areas of Dry Regions, Year 3, Numbers 9 and 10, Autumn and Winter 1391.
22. Mani, A., & Hosseini Shamchi, A. (1389). Investigation of Wind Energy Potential in Stations of the South Ahar River Basin. Geographical Space Scientific Research Journal, 10(29), Spring.
23. Broumand, M. (1380). Wind Energy Density. Neyvar Journal, Numbers 42 and 43.
24. Jamil, M. (1375). Application of Wind Turbines in Germany. Iran Energy Journal, September.
25. Jahangiri, et al. (1384). Calculation of Wind Energy Using Two-Parameter Weibull Distribution. Geographical Research Quarterly, 20th Year, Number 76.
26. Renewable Energy Organization of Iran (SANAE). (1391). Retrieved from http://www.sana.ir
27. Shamsabad, A. H. (1379). Investigation of Wind Energy Utilization in Various Climatic Conditions of Iran. Fourth National Conference on Rural and Efficient Energy, Chabahar.
28. Azizi, M., & Jahangirian, A. (2020). Multi-Site Aerodynamic Optimization of Wind Turbine Blades for Maximum Annual Energy Production in East Iran. Energy Science & Engineering Journal, 8, 169–186. https://doi.org/10.1002/ese3.763.
29. Ai, Q., Weaver, P. M., Barlas, T. K., Olsen, A. S., Madsen, H. A., & Andersen, T. L. (2019). Field testing of morphing flaps on a wind turbine blade using an outdoor rotating rig. Renewable Energy, 133, 53–65.
30. McWilliam, K. M., Thanasis, K., Madsen, A. H., & Zahle, F. (2018). Aero-elastic wind turbine design with active flaps for AEP maximization. Wind Energy Science, 3(1), 231–241.
31. Saenz-Aguirre, A., Fernandez-Resines, S., Aramendia, I., Fernandez-Gamiz, U., Zulueta, E., Lopez-Guede, J. M., & Sancho, J. (2018). 5 MW Wind Turbine Annual Energy Production Improvement by Flow Control Devices. Proceedings, 2(23), 1452.
32. Zhang, Y., Ramdoss, V., Saleem, Z., Wang, X., Schepers, G., & Ferreira, C. (2019). Effects of root Gurney flaps on the aerodynamic performance of a horizontal axis wind turbine. Energy, 187.
33. Branlard, E. (2020). Wind Turbine Aerodynamics and Vorticity-Based Methods. Springer.
34. Nasir, H. F. (1398). What is a Wind Tunnel.
35. Samaei, S. R., Ghodsi Hassanabad, M. (2021). Numerical and experimental investigation of damage in environmentally-sensitive civil structures using modal strain energy (case study: LPG wharf).

International Journal of Environmental Science and Technology, 18, 1939–1952. https://doi.org/10.1007/s13762-021-03321-2

36. Samaei, S. R., Azarsina, F., & Ghahferokhi, M. A. (2016). Numerical simulation of floating pontoon breakwater with ANSYS AQWA software and validation of the results with laboratory data. Bulletin de la Société Royale des Sciences de Liège, 85, 1487-1499.
37. Samaei, S. R., & Ghodsi Hassanabad, M. (2022). Damage location and intensity detection in tripod jacket substructure of wind turbine using improved modal strain energy and genetic algorithm. Journal of Structural and Construction Engineering, 9(4), 182-202. https://doi.org/10.22065/jsce.2021.294103.2488
38. Samaei, S. R., Ghodsi Hassanabad, M., Asadian Ghahfarrokhi, M., & Ketabdari, M. J. (2021). Numerical and experimental study to identify the location and severity of damage at the pier using the improved modal strain energy method-Case study: Pars Asaluyeh LPG export pier. Journal of Structural and Construction Engineering, 8(Special Issue 3), 162-179. https://doi.org/10.22065/jsce.2020.246425.2225
39. Samaei, S. R., Ghodsi Hassanabad, M., Asadian Ghahfarrokhi, M., & Ketabdari, M. J. (2020). Structural health monitoring of offshore structures using a modified modal strain energy method (Case study: four-leg jacket substructure of an offshore wind turbine). Journal Of Marine Engineering, 16(32), 119-130.
40. Samaei, S. R., Ghodsi Hassanabad, M., & Karimpor Zahraei, A. (2021). Identification of Location and Severity of Damages in the Offshore wind Turbine Tripod Platform by Improved Modal Strain Energy Method. Analysis of Structure and Earthquake, 18(3), 51-62.
41. Samaei, S. R., Ghodsi Hassanabad, M., Asadian Ghahfarrokhi, M., & Ketabdari, M. J. (2021). Investigation of location and severity of damage in four-legged offshore wind turbine stencil infrastructure by improved modal strain energy method. Analysis of Structure and Earthquake, 17(3), 79-90.
42. Samaei, S. R., Azarsina, F., & Ghahferokhi, M. A. (2016). Numerical simulation of floating pontoon breakwater with Ansys Aqua software and validation of results with laboratory data. The third national conference on recent innovations in civil engineering, architecture and urban planning.